Spherical tarball particles form through rapid chemical and physical changes of organic matter in biomass-burning smoke

Kouji Adachi[a,1], Arthur J. Sedlacek III[b], Lawrence Kleinman[b], Stephen R. Springston[b], Jian Wang[b,c], Duli Chand[d], John M. Hubbe[d], John E. Shilling[d], Timothy B. Onasch[e], Takeshi Kinase[a], Kohei Sakata[f], Yoshio Takahashi[g], and Peter R. Buseck[h,i]

[a]Department of Atmosphere, Ocean and Earth System Modeling Research, Meteorological Research Institute, 3050052 Tsukuba, Japan; [b]Environmental and Climate Sciences, Brookhaven National Laboratory, Upton, NY 11973; [c]Center for Aerosol Science and Engineering, Department of Energy, Environmental and Chemical Engineering, Washington University in St. Louis, St. Louis, MO 63130; [d]Atmospheric Sciences and Global Change Division, Pacific Northwest National Laboratory, Richland, WA 99352; [e]Center for Sensor Systems and Technology, Aerodyne Research Inc., Billerica, MA 01821; [f]Center for Global Environmental Research, National Institute for Environmental Studies, 3058506 Tsukuba, Japan; [g]Graduate School of Science, The University of Tokyo, 1130033 Tokyo, Japan; [h]School of Earth and Space Exploration, Arizona State University, Tempe, AZ 85287; and [i]School of Molecular Sciences, Arizona State University, Tempe, AZ 85287

Edited by Mark H. Thiemens, University of California San Diego, La Jolla, CA, and approved August 16, 2019 (received for review January 4, 2019)

Biomass burning (BB) emits enormous amounts of aerosol particles and gases into the atmosphere and thereby significantly influences regional air quality and global climate. A dominant particle type from BB is spherical organic aerosol particles commonly referred to as tarballs. Currently, tarballs can only be identified, using microscopy, from their uniquely spherical shapes following impaction onto a grid. Despite their abundance and potential significance for climate, many unanswered questions related to their formation, emission inventory, removal processes, and optical properties still remain. Here, we report analysis that supports tarball formation in which primary organic particles undergo chemical and physical processing within ∼3 h of emission. Transmission electron microscopy analysis reveals that the number fractions of tarballs and the ratios of N and O relative to K, the latter a conserved tracer, increase with particle age and that the more-spherical particles on the substrates had higher ratios of N and O relative to K. Scanning transmission X-ray spectrometry and electron energy loss spectrometry analyses show that these chemical changes are accompanied by the formation of organic compounds that contain nitrogen and carboxylic acid. The results imply that the chemical changes increase the particle sphericity on the substrates, which correlates with particle surface tension and viscosity, and contribute to tarball formation during aging in BB smoke. These findings will enable models to better partition tarball contributions to BB radiative forcing and, in so doing, better help constrain radiative forcing models of BB events.

tarball | biomass burning | climate change | organic aerosol | transmission electron microscopy

Biomass burning (BB) events exert a significant influence on regional air quality and potentially on global climate (1–3) since they are a major source of gases, black carbon (BC), and organic carbon including light-absorbing organic particles commonly referred to as brown carbon (BrC) (4, 5). It is estimated that BB events account for 50% of anthropogenically influenced fine carbonaceous particles (6–8). In coming decades, emissions from BB events are expected to increase in the western United States (9) and possibly globally (10) due to climate change caused by human activity. However, despite the atmospheric abundance from BB emissions, the radiative forcing and potential climate impacts of BB aerosol particles remain highly uncertain (11).

Several groups have documented the occurrence of spherical organic particles, referred to as tarballs (12), in BB smoke across the globe (13–17). In BB smoke and haze, these tarballs can dominate the aerosol particle types examined using electron microscopy (14, 15) and have been estimated to contribute up to ∼30% of the BB aerosol mass (18), which indicates that tarballs could be a major BB aerosol particle type in the global atmosphere. A model study (19) suggests that the global hydrometer mass absorption coefficient of tarball can be half of BC at a wavelength of 650 nm when assuming that tarballs are strongly light-absorbing particles (20).

Despite their potential major contribution to the global climate, we know little about tarballs, and there is no consensus regarding their formation mechanism, emission inventory, removal process, and optical properties. Studies to understand tarball fundamental properties found that they possess unique optical and physical features such as a broad spectral absorption that spans from the shortwave spectral region (<400 nm) to the near infrared (15, 21, 22) and extremely low volatility (23). When number concentrations are high, tarball aggregates are potentially responsible for an increase of single-scattering albedo by up to 40% (17). Finally, studies have evaluated the imaginary part of the tarball refractive index as having a wide range, from 0.002 to 0.27 (18), which leaves significant uncertainties about tarball optical properties.

Various tarball formation mechanisms have been proposed to explain both field observations (14, 16–18, 24, 25) and laboratory

Significance

Wildfires emit large amounts of biomass-burning (BB) aerosol particles and contribute to regional and global climate. Moreover, BB emissions are expected to increase in coming decades as a result of climate change. Tarballs, spherical organic BB particles, are estimated to contribute up to ∼30% of the BB aerosol mass. However, uncertainty still exists as to how tarballs form and how they influence climate. Our observations show that tarballs form through a combination of chemical and physical changes of primary organic aerosols within the first hours following emission. The finding of tarball formation will improve assessments of BB particle evolution and of BB impacts on regional and global climate.

Author contributions: K.A., A.J.S., L.K., and P.R.B. designed research; K.A., A.J.S., L.K., S.R.S., J.W., D.C., J.M.H., J.E.S., T.B.O., T.K., K.S., and Y.T. performed research; K.A., A.J.S., L.K., S.R.S., J.W., D.C., T.B.O., K.S., and Y.T. analyzed data; and K.A., A.J.S., L.K., T.B.O., and P.R.B. wrote the paper.

The authors declare no conflict of interest.

This article is a PNAS Direct Submission.

[1]To whom correspondence may be addressed. Email: adachik@mri-jma.go.jp.

This article contains supporting information online at www.pnas.org/lookup/suppl/doi:10.1073/pnas.1900129116/-/DCSupplemental.

First published September 5, 2019.

experiments (22, 26, 27), and the subject thus remains an active area of research. Polymerization of organic matter, condensation, photochemical processes, loss of water, heat shock, and temperature changes have all been proposed to contribute to tarball formation. The goal of this study is to elucidate tarball formation by examining how the chemical and physical features of BB aerosol particles change with time and, in turn, to provide an improved quantitative understanding of the contribution of tarballs to regional and global climate.

Results

Physical and Chemical Features of Tarballs. Tarballs used in this study were collected from large wildfires sampled during the Biomass Burning Observation Project (BBOP) in the summer of 2013 in the northwestern United States. Using a Gulfstream-1 (G-1) research aircraft (28), we collected BB aerosol particles on transmission electron microscopy (TEM) grids. Shape and chemical composition of more than 10,000 particles were measured using TEM, with detailed chemical-state analysis of tarballs performed using scanning transmission X-ray spectroscopy (STXM). In this current study, we focus on 3 fires sampled during 4 research flights (*SI Appendix*, Table S1). Samples from these fires allowed us to conduct a detailed study of how the microphysical and chemical properties of tarballs evolve with time following ∼3 h of aging from emission. Tarball number fractions were nearly zero for young smoke with photochemical age of <0.5 [photochemical age: $-\log_{10}(NO_x/NO_y)$ (29)] for smoke from all 3 fires (Fig. 1) but increased rapidly by up to ∼80% by number for smoke with photochemical age of >0.5 (∼1 h or more from the emission).

TEM analysis shows that tarballs appear spherical on TEM grids, possess modal diameters of ∼220 nm (σ = 1.6), and are amorphous (Fig. 2), consistent with observations in other studies (13–17). The shape and structure of tarballs differ from those of nanosphere soot (ns-soot, i.e., soot defined using TEM) particles. Specifically, ns-soot particles consist of aggregates of ∼40-nm nanospheres that possess distinctive structures of concentrically wrapped, graphene-like layers of carbon with ∼0.35-nm spacings (30), whereas tarball particles are amorphous, without graphene-like layers (Fig. 2*B* and *SI Appendix*, Fig. S2). TEM images from this study and others suggest that tarballs do not embed in or coat on ns-soot particles, and that their mixing state differs from many secondary organic aerosol (SOA) particles (31).

Functional groups within tarballs were determined using STXM (*SI Appendix*, Fig. S1). The results show that tarballs have absorption peaks at 285.2 eV (peak identified as 1), 286.7 eV (peak 2), and 288.5 eV (peak 3), which correspond to aromatic, ketonic or phenolic, and carboxylic carbon, respectively. These functional groups have also been identified in tarballs from other locations (32–34), which indicates that these functional groups are common in tarballs.

The shapes of particles collected on TEM substrates using an impactor sampler depend on particle viscosity, including elastic and liquid flow properties and surface tension (35), and differ significantly between fresh and aged BB samples (Fig. 3). For example, when particles are collected near a fire (fresh samples), they spread over the substrate, which indicates that they had low viscosity and surface tension. In contrast, as they age in the smoke plume, their viscosity and surface tension increase, and they ultimately appear spherical on TEM substrates and become recognizable as tarballs (*SI Appendix*, Fig. S3). For example, Reid et al. (25) reviewed the viscosities of spherical organic particles on a substrate as ranging between 10^9 Pa·s and 10^{12} Pa·s, whereas those of liquid particles are between 10^{-1} Pa·s and 10^2 Pa·s.

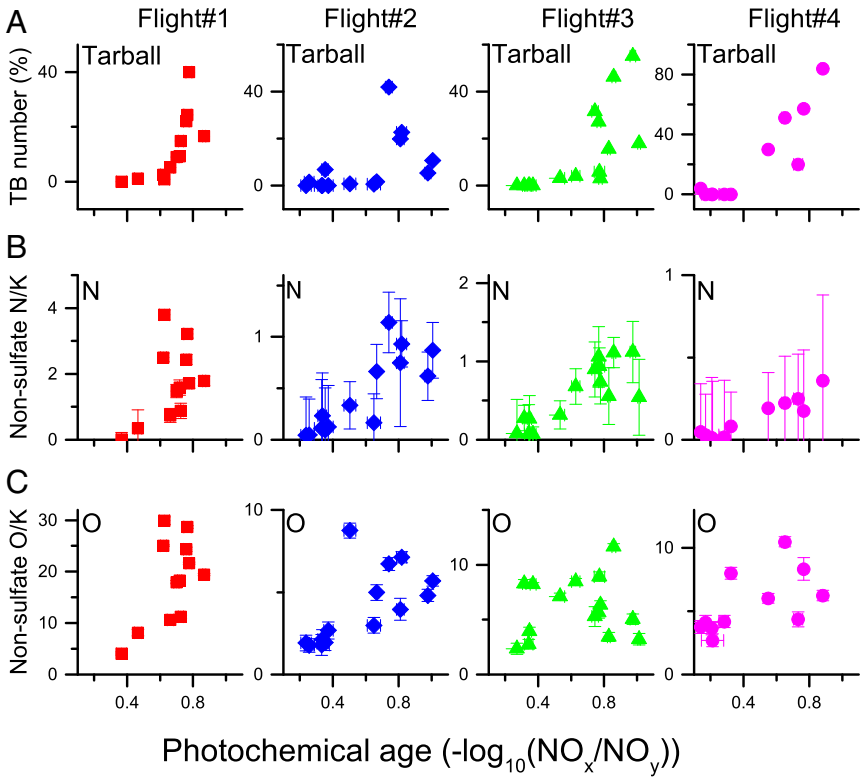

Fig. 1. Changes of (*A*) tarball (TB) number fractions, (*B*) nonsulfate N/K within nontarball particles, and (*C*) nonsulfate O/K within nontarball particles as photochemical ages increase for each flight. Error bars indicate the 95% confidence intervals. Numbers of measured nontarball particles for the EDS analyses are 2,451, 3,271, 1,962, and 2,085 for flights 1, 2, 3, and 4, respectively. Averaged values of nonsulfate N/K of tarballs are 6.7 ± 0.1, 2.9 ± 0.3, 2.2 ± 0.2, and 0.9 ± 0.2 and those of O/K are 47.6 ± 0.1, 14.1 ± 0.3, 9.9 ± 0.2, and 10.4 ± 0.3 for flights 1, 2, 3, and 4, respectively. All ratios are calculated from weight percentage values.

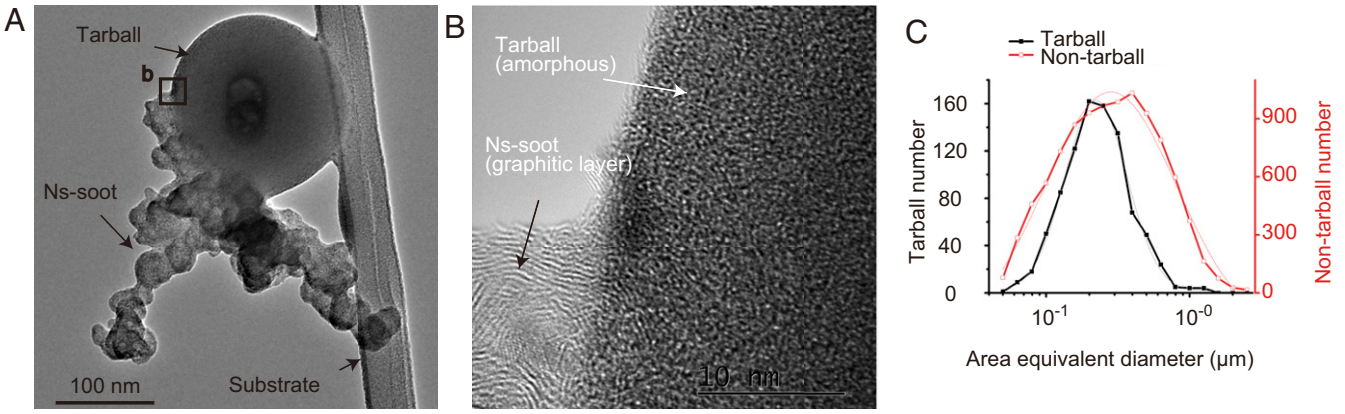

Fig. 2. Shape, structure, and size of tarballs. (*A*) Tarball particle with attached ns-soot and resting on the substrate (linear fiber). (*B*) High-resolution TEM image of the tarball and ns-soot in box in *A*. (*C*) Size distributions of tarballs (n = 894) and nontarball particles (n = 9,878) from all measured TEM samples. The mode diameters obtained from log-normal peak fits (dotted lines) are 223 nm (σ = 1.6) and 282 nm (σ = 2.4) for tarballs and nontarball particles, respectively.

Aerosol particles from BB smoke consist of various organic compounds that also contain potassium salts, sulfate, nitrate, and ns-soot particles. Energy-dispersive X-ray spectrometer (EDS) maps created using scanning TEM (STEM) of fresh BB samples (~0.5 h from the emission) indicate that grains of potassium sulfate and chloride occur within BB organic particles (*SI Appendix*, Fig. S4). A prior study (36) showed that KCl in BB particles was chemically transformed into K_2SO_4 within the first ~8 km downwind of a BB fire. As we found K_2SO_4 dominated the BB particles in our fresh samples collected ~10 km downwind from the fire, it is possible that KCl particles were originally emitted, but Cl could have been replaced by sulfate and released gaseous HCl (36). Particles in moderately aged samples (~1 h from emission) include 1 or 2 potassium sulfate grains per particle, and Cl is homogeneously distributed throughout the particles. Tarballs dominate in the most aged samples (~2 h from emission) and are characterized by uniform distributions of C, O, and N throughout the particles, with potassium sulfate in some particles.

Nitrogen is uniformly distributed within the BB organic particles (Fig. 3 and *SI Appendix*, Fig. S4). The distribution of N-containing compounds differs from that of ammonium sulfate, which occurs as crystalline grains that decompose under a strong electron beam (37). Electron energy loss spectrometry (EELS) analysis also shows that the chemical states of N within tarballs differ from ammonium sulfate (*SI Appendix*, Fig. S5). Stoichiometry calculations from the STEM-EDS analysis of the nonvolatile particles show that only about 14 ± 3% of the N-bearing compounds occur as ammonium sulfate. Instead, the dominant form of nonvolatile N is associated with organic matter. Various organic nitrogen compounds (ONC) have been reported from BB aerosol particles (34, 38) and in tarballs by using STXM (32). These results suggest that N occurs as either an organic nitrate or nitroaromatic.

Individual Particle Composition as a Function of Photochemical Age. Using ratios of the relative weight percent of specific elements to K, a conserved tracer (*SI Appendix*, Fig. S6 and *SI Text*), we find that nonsulfate N/K and nonsulfate O/K (hereafter simply "N/K" and "O/K") increased with age concomitantly with an increase in the tarball number fraction (Fig. 1). The extent of these increases is similar within the same BB wildfire (flights 2 and 3) but varies among different wildfires, possibly due to different source fuels (39) and burn conditions. Tarballs have also higher ratios in N/K and O/K than nontarball particles (Fig. 4). The N/K and O/K values of tarballs from each fire generally correlate with those of other particles, i.e., flight 1 has the highest values for both tarballs and nontarballs, whereas flight 4 has the lowest values for both. Thus, although N/K and O/K values differ among BB smokes, the increases of these ratios seem general and are key in tarball formation, as discussed below.

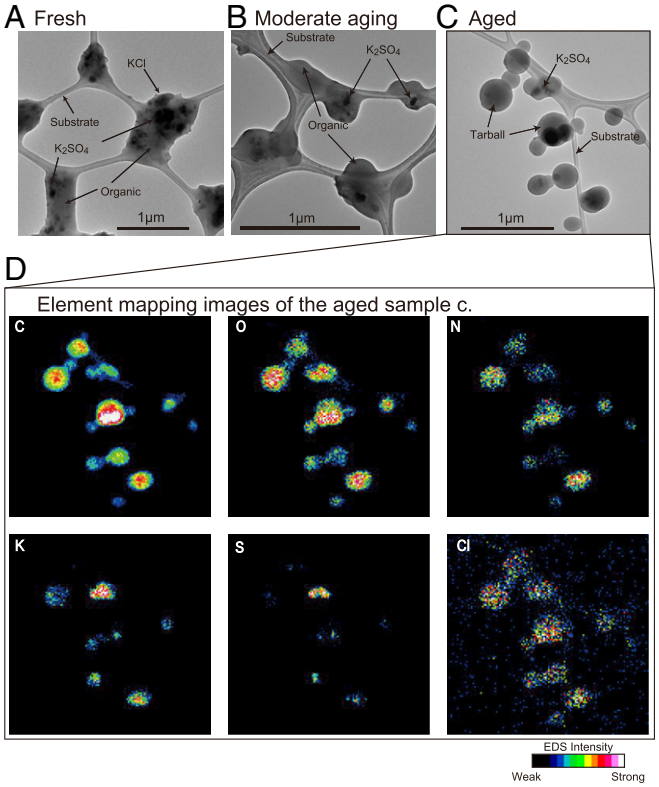

Fig. 3. Particle shape changes and element distributions in an aged sample from flight 3. (*A*) TEM image of fresh BB sample with photochemical age of 0.34. Many grains of K_2SO_4 and KCl as well as ns-soot are embedded within organic matter spread over the substrate. (*B*) TEM image of moderately aged sample with photochemical age of 0.62. Particles have increased viscosities and appear round but not spherical. (*C*) TEM image of aged sample with photochemical age of 0.97. Particles have become spherical, and the tarball number fraction increased. (*D*) Element mapping images of the TEM image in *C*. C, O, N, and Cl occur in all particles, whereas K and S are embedded within some tarballs or other OA particles and appear as dark inclusions in the TEM image in *C*. Colors indicate normalized EDS intensities for each element.

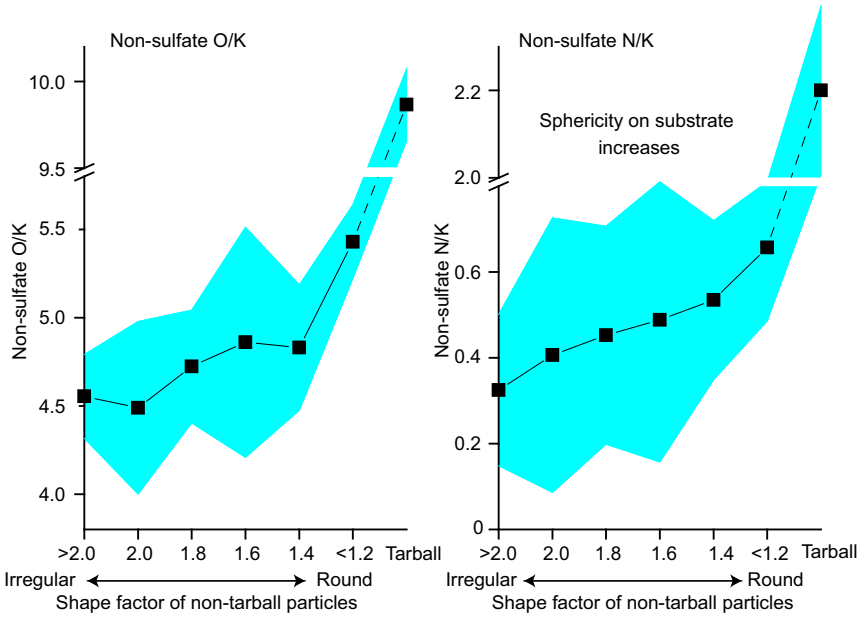

Fig. 4. Increases of nonsulfate N/K and O/K as particle shape factors decrease. Averaged shape factors are 1 for a sphere and increase for irregular particles. In general, the higher the viscosity and surface tension of OA particles, the lower the shape factors, because they can retain their spherical shapes on the substrate. Low viscous OA particles have lower N/K and O/K and higher shape factors. The colored area indicates the 95% confidence interval. The dashed lines show extrapolations to tarballs. The plots are for all samples from flight 3. All ratios are calculated from weight percentage values.

Compositional changes were also observed with the Soot Particle Aerosol Mass Spectrometer (SP-AMS), which indicated an increase of O/C for the BBOP samples (*SI Appendix*, Fig. S6). The O/C ratios for flight 3 increased from 0.2 to 0.4 within ∼2.5 h. Such increases have been observed in other BB smokes. For example, Zhou et al. (40) showed an increase of O/C in the BB OAs as cumulative solar radiation increased. The O/C increase also agrees with the rapid changes by photochemical oxidation of wood fire in chamber experiments (41), and the results were incorporated in the 2D volatility basis set (42). Finally, recent studies (43, 44) report that nitroaromatic compounds, a marker for ONC, increased in various BB smokes upon aging, which is consistent with our results.

Tarball Formation. We propose that the increase in organic matter viscosity and surface tension with tarball formation in the analyzed BB plumes proceeds by the addition of O and N in initially low-viscosity organic particles by formation of, for example, carboxylic acid and ONC within several hours from emission. Although tarballs are several times higher in O/K and N/K than nontarball particles, the latter, when they have round shapes on the substrates, have higher ratios than those having irregular shapes (Fig. 4). The relationship between particles' shape and composition is also observed within samples having similar photochemical ages, i.e., samples having photochemical age of >0.5 and those <0.5.

Sedlacek et al. (18) proposed that tarballs formed through secondary processes within primary particles and referred to these particles as processed primary particles. Our findings support this designation. In addition, condensation of SOA particles could also contribute to particle formation, especially in fresh smoke (photochemical age of <0.5) where particle size increased rapidly (*SI Appendix*, Fig. S8). For aged samples, since we observed increases neither of particle size nor of OA mass (18) with particle age, the secondary processes within primary particles seemingly dominate the particle chemical and physical changes.

The proposed tarball formation mechanism is consistent with bulk observations of BB OA evolution. For example, Jimenez et al. (45) showed that BB emissions evolve by becoming increasingly oxidized and less volatile, forming oxygenated OA. Studies also measured rapid chemical processing of OA from BB smoke in laboratory experiments (39) and in ambient smoke (46). These rapid changes of chemical compositions are common in many BB smokes, and our study suggests that such changes could also lead to the physical changes, i.e., increases in viscosity and surface tension, that accompany tarball formation. The change in viscosity can also affect gas-to-particle reactions by changing the molecular diffusion rates in the primary particles from BB emissions (47, 48).

Particulate ammonium and nitrate materials, as well as gaseous nitrogen oxides, were higher within the BB plume than in the background air during the BBOP campaign (40, 49). These N-containing compounds could coagulate with organic matter or react with low-viscosity organic particles (47). Although temperature and relative humidity (RH) can influence aerosol particle viscosity (50), these values in the BB smoke in our measurements did not change significantly (temperature < 24 °C and RH < 60%; see *SI Appendix*, Fig. S6), suggesting that the observed changes in viscosity and surface tension were primarily driven by chemical reactions.

Summary and Climate Implications. It is becoming ever clearer that tarballs are an important particle type generated by wildfires. Their importance dictates that we should better quantify their chemical, microphysical, and optical properties so that their contributions to aerosol radiation forcing can be better understood and constrained in climate models.

In this study, we show that increases in the N/K and O/K values correlate with particle shapes on the substrates and tarball formation at the individual particle scale. This correlation suggests that chemical reactions involving O and N with primary OA (POA) change the particle viscosity and surface tension and result in tarballs. From our observations, changes of temperature, loss of water, or heat shock during emission are less likely to contribute to tarball formation than the chemical reactions. Further studies are needed to confirm the quantitative relations between the addition of N and O and microphysical properties

(e.g., viscosity and surface tension) with particle age. Oxidation can also change the particle hygroscopicity (45, 51) through the formation of, for example, carboxyl acid. However, measurements of tarball hygroscopicity vary (15, 16, 52), and the issue remains open.

Formation of ONC can increase particle light absorption at short wavelengths, producing BrC (38, 53). The shortwave light absorption occurs because N atoms can be coupled to double bonds and become effective chromophores through $\pi-\pi^*$ and $n-\pi^*$ transitions (54). Light absorption by BrC becomes larger at shorter wavelengths (e.g., <500 nm) (24) and changes depending on its mixing states (5). Carbon sp2 hybridization (C=C) observed using EELS and STXM analyses of peaks near 285 eV can also contribute to light absorption (33) (*SI Appendix*, Figs. S1 and S5).

The measured single-scattering albedo at a wavelength of 550 nm showed no increase of light absorption during the formation of tarballs in BBOP flight 3 (18). The tarballs observed in the BBOP campaign exhibited light absorption that was more in line with that expected for BrC particles at the observed wavelength (<0.02 for the imaginary part of the refractive index). The weak tarball absorption generally falls within the range of ONC absorption values in other studies (54), although further oxidation (>0.7 d) could diminish tarball absorption by bleaching (27).

In summary, tarballs form a distinct class of organic particles based on their shape and underlying unique physical and chemical features, which include 1) spherical shape following impaction onto a grid, 2) ∼220-nm diameter with a relatively wide distribution ($\sigma = 1.6$), and 3) relatively high ratios in N/K (>∼1) and O/K (>∼10). Our chemical and microphysical analyses of BB aerosol particles reveal the roles of oxygen and nitrogen uptake in transforming POA with low viscosity and surface tension to the tarballs with high viscosity and surface tension.

Tarballs have been a unique aerosol type that has a spherical shape following impaction onto a TEM grid. Since tarballs are estimated to be a dominant, light-absorbing type of aerosol particle from BB smoke, understanding their climate influences is crucial. This study reveals their formation process through chemical and microphysical analyses. The findings can be used to improve retrieval of BB smoke from satellite data and ground-based observations by considering tarballs' shape, viscosity, surface tension, and compositional changes during aging and to provide better estimates of the radiative forcing in climate models.

Materials and Methods

Sampling Campaign and Instruments. An aircraft measurement, BBOP campaign was conducted in the northwestern United States (23, 40, 49, 55). The first period of this campaign was based in Washington, Oregon, and Idaho from July to September 2013 to collect BB smoke from wildfires. We used online data from a 3-channel chemiluminescent instrument (Air Quality Design, Model 1) for the oxides of nitrogen (e.g., NO, NO_x, NO_y), an intracavity off-axis spectroscope (Los Gatos, Model 907) for CO measurements, an SP-AMS (Aerodyne Research Inc.) for the nonrefractory particulate matter mass analyses (56), and a fast integrated mobility spectrometer for aerosol particle size measurements (57) (*SI Appendix*, Fig. S8). Details of these online instruments for aerosol and gas measurements are described elsewhere (18, 28, 49, 55). The photochemical age of the smoke was calculated using the ratio of NO_x to NO_y, $-\log_{10}(NO_x/NO_y)$ (18, 29).

For the TEM analysis, we collected aerosol particles on lacey carbon TEM grids (Ted Pella, Type 01881 [200 mesh]) using an impactor sampler (AWS-16, Arios) (23, 37, 58) that can load 16 TEM grids attached to an aluminum plate for each impactor stage (see *SI Appendix, SI Text* for details of the sampling).

Fifteen or 16 samples ranging from fresh to relatively aged (∼3 h emission) per flight were collected for flights on 26 and 30 July and 21 August (*SI Appendix*, Table S1). Among the 59 TEM samples collected during the flights, we used 52 TEM samples having CO concentrations higher than the background air (CO > 0.112 parts per million by volume) as BB samples. Ambient temperature varied depending on the flight altitude and ranged from 4 °C to 24 °C, and the RH values were under 60% during the flights (*SI Appendix*, Fig. S7). The BB smokes in this study were mostly sampled during flaming combustion (55), and the fuels were timber, brush, and grass.

TEM and Composition Analysis. To analyze shape, size, and composition of individual particles, we used a transmission electron microscope (JEM-1400, JEOL) with EDS (X-max 80 mm, Oxford Instruments). Particle composition was analyzed using the STEM mode with a semiautomatic particle measurement system (58) (see *SI Appendix, SI Text* for the particle measurement). We analyzed ∼200 particles from each grid for a total of 10,772 particles from 52 TEM samples. We also identified tarball particles from the TEM images for the particles used for the EDS analyses.

The vapor pressure of volatile and semivolatile organic and inorganic compounds in the sample chamber was too high to retain them in the particles (40, 59, 60), resulting in the loss of the volatile fraction from the particles collected on the TEM grids. We compared nonsulfate N and nonsulfate O weight percentages averaged within all particles in each sample divided by the K average weight percent (sample ensemble average) to normalize the decrease of C caused by the loss of volatile compounds from the fresh samples (*SI Appendix, SI Text*).

Tarball number fractions were measured using representative TEM images with ∼200 particles in each sample. We counted as tarballs only spherical, organic particles that display no deformation on the substrates, i.e., shape factor of <1.1. Some droplet particles can appear round on the substrate, but they have weaker contrast than tarballs because of flattened shapes on the substrate and were excluded from the tarball category. Such flattened shapes can also be recognized in tilted images (*SI Appendix*, Fig. S9). There were many probable tarball precursor particles in relatively fresh samples that had nearly spherical shapes and similar compositions but were slightly deformed on the substrate; however, we excluded them from the tarball category unless they agreed with the tarball definition mentioned above.

High-resolution images and EELS spectra were obtained to estimate the chemical states of C and N within tarballs. For this purpose, we used TEM (JEM-ARM200F) with a cold field emission gun and an aberration-corrected column equipped with EELS (GATAN Quantum). We also measured functional groups of the near-edge X-ray absorption fine structure spectra of the tarballs at the C–K edge using STXM at the Photon Factory of the High Energy Accelerator Research Organization (KEK) using the method and reference materials of fulvic acid and humic acid described in Takahashi et al. (61).

Nitrogen and O can be from both organic and nonorganic compounds such as ONC, ammonia, nitrate, or ammonium sulfate. We evaluated the weight percentages of N and O from ammonium sulfate and nonammonium sulfate. Here, N in ammonium sulfate was identified assuming that all Cl, K, and S in aerosol particles occur as follows: [Cl] = KCl; [K] = KCl + K_2SO_4; [S] = K_2SO_4 + $(NH_4)_2SO_4$; [N] = $(NH_4)_2SO_4$ + [nonammonium sulfate N]. The nonammonium sulfate N can include ammonium, nitrate, and ONC. Oxygen in nonsulfate was retrieved by removing O in sulfate, i.e., [all O] – [O in sulfate] = [nonsulfate O]. Errors for S, Cl, and K are 8%, 12%, and 5%, respectively, based on the averaged values from the X-ray peak intensity sigma for each element. The uncertainties for N and O were evaluated as <5% using laboratory-generated aerosol particles with mixtures of potassium sulfate, ammonium sulfate, and phthalic acid (*SI Appendix*, Fig. S10).

Data Availability. Data from the BBOP campaign are publicly available at the Department of Energy Atmospheric Radiation Measurement (DOE ARM) user facility data center (https://adc.arm.gov/discovery/) with registration to the website.

ACKNOWLEDGMENTS. This research was supported by the ARM user facility, a US DOE Office of Science user facility managed by the Office of Biological and Environmental Research. We acknowledge the DOE ARM user facility for both the support to carry out the BBOP campaign and use of the G-1 research aircraft. We gratefully acknowledge the skill and safety exemplified by the ARM Aerial Facility pilots and flight staff. K.A. acknowledges the support of the Environment Research and Technology Development Fund (Grants 2-1403, 5-1605, and 2-1703) of the Environmental Restoration and Conservation Agency and the Grants-in-Aid for Scientific Research by the Japan Society for the Promotion of Science (KAKENHI) (Grants JP25740008, JP16K16188, JP16H05620, JP15H02811, JP16H01772, JP19H04259, and JP18H04134). The EELS study was supported by the National Institute for Materials Science (NIMS) microstructural characterization platform as a program of the "Nanotechnology Platform" of the Ministry of Education, Culture, Sports, Science and Technology, Japan. The STXM analysis was performed with the approval of KEK (Proposals 2013S2-003 and 2016S2-002). We acknowledge

Dr. Y. Nemoto (NIMS) for his help in using the TEM (ARM), Mr. H. Suga for the STXM measurements of reference materials, and Dr. M. Pekour (Pacific Northwest National Laboratory [PNNL]) and Dr. E. Fortner (Aerodyne) for the SP-AMS measurements. A.J.S., L.K., and T.B.O. acknowledge research support by the US DOE Office of Biological & Environmental Research, Atmospheric System Research program under Contracts DE-SC0012704 (Brookhaven National Laboratory; A.J.S. and L.K.), KP1701000/57131 (PNNL, J.E.S.), and DE-SC0014287 (T.B.O.). D.C., J.E.S., and J.M.H. acknowledge support from the ARM user facility through PNNL, which is operated for DOE by Battelle Memorial Institute under Contract DE-AC06-76RLO1830. P.R.B. acknowledges support from PNNL and the DOE ARM under 305 Research Subcontract 20568.

1. S. K. Akagi *et al*., Emission factors for open and domestic biomass burning for use in atmospheric models. *Atmos. Chem. Phys.* **11**, 4039–4072 (2011).
2. T. C. Bond *et al*., Bounding the role of black carbon in the climate system: A scientific assessment. *J. Geophys. Res. Atmos.* **118**, 5380–5552 (2013).
3. C. D. McClure, D. A. Jaffe, US particulate matter air quality improves except in wildfire-prone areas. *Proc. Natl. Acad. Sci. U.S.A.* **115**, 7901–7906 (2018).
4. R. Saleh *et al*., Brownness of organics in aerosols from biomass burning linked to their black carbon content. *Nat. Geosci.* **7**, 647–650 (2014).
5. R. M. Saleh *et al*., Contribution of brown carbon and lensing to the direct radiative effect of carbonaceous aerosols from biomass and biofuel burning emissions. *J. Geophys. Res. Atmos.* **120**, 10,285–10,296 (2015).
6. T. C. Bond *et al*., A technology-based global inventory of black and organic carbon emissions from combustion. *J. Geophys. Res. Atmos.* **109**, D14203 (2004).
7. M. O. Andreae, D. Rosenfeld, Aerosol–cloud–precipitation interactions. Part 1. The nature and sources of cloud-active aerosols. *Earth Sci. Rev.* **89**, 13–41 (2008).
8. J. de Gouw, J. L. Jimenez, Organic aerosols in the Earth's atmosphere. *Environ. Sci. Technol.* **43**, 7614–7618 (2009).
9. J. T. Abatzoglou, A. P. Williams, Impact of anthropogenic climate change on wildfire across western US forests. *Proc. Natl. Acad. Sci. U.S.A.* **113**, 11770–11775 (2016).
10. B. J. Harvey, Human-caused climate change is now a key driver of forest fire activity in the western United States. *Proc. Natl. Acad. Sci. U.S.A.* **113**, 11649–11650 (2016).
11. O. Boucher *et al*., *Climate Change 2013: The Physical Science Basis*, T. F. Stocker *et al*., Eds. (Cambridge Univ. Press, 2013), pp. 571–658.
12. M. Pósfai, R. Simonics, J. Li, P. V. Hobbs, P. R. Buseck, Individual aerosol particles from biomass burning in southern Africa: 1. Compositions and size distributions of carbonaceous particles. *J. Geophys. Res. Atmos.* **108**, 8483 (2003).
13. S. China, C. Mazzoleni, K. Gorkowski, A. C. Aiken, M. K. Dubey, Morphology and mixing state of individual freshly emitted wildfire carbonaceous particles. *Nat. Commun.* **4**, 2122 (2013).
14. M. Pósfai *et al*., Atmospheric tar balls: Particles from biomass and biofuel burning. *J. Geophys. Res. Atmos.* **109**, D06213 (2004).
15. J. L. Hand *et al*., Optical, physical, and chemical properties of tar balls observed during the Yosemite Aerosol Characterization Study. *J. Geophys. Res. Atmos.* **110**, D21210 (2005).
16. K. Adachi, P. R. Buseck, Atmospheric tar balls from biomass burning in Mexico. *J. Geophys. Res. Atmos.* **116**, D05024 (2011).
17. G. Girotto *et al*., Fractal-like tar ball aggregates from wildfire smoke. *Environ. Sci. Technol. Lett.* **5**, 360–365 (2018).
18. A. J. Sedlacek III *et al*., Formation and evolution of tar balls from Northwestern US wildfires. *Atmos. Chem. Phys.* **18**, 11289–11301 (2018).
19. M. Z. Jacobson, Investigating cloud absorption effects: Global absorption properties of black carbon, tar balls, and soil dust in clouds and aerosols. *J. Geophys. Res. Atmos.* **117**, D06205 (2012).
20. D. T. Alexander, P. A. Crozier, J. R. Anderson, Brown carbon spheres in East Asian outflow and their optical properties. *Science* **321**, 833–836 (2008).
21. R. K. Chakrabarty *et al*., Brown carbon in tar balls from smoldering biomass combustion. *Atmos. Chem. Phys.* **10**, 6363–6370 (2010).
22. A. Hoffer, A. Tóth, I. Nyirő-Kósa, M. Pósfai, A. Gelencsér, Light absorption properties of laboratory-generated tar ball particles. *Atmos. Chem. Phys.* **16**, 239–246 (2016).
23. K. Adachi *et al*., Volume changes upon heating of aerosol particles from biomass burning using transmission electron microscopy. *Aerosol Sci. Technol.* **52**, 46–56 (2018).
24. A. Laskin, J. Laskin, S. A. Nizkorodov, Chemistry of atmospheric brown carbon. *Chem. Rev.* **115**, 4335–4382 (2015).
25. J. P. Reid *et al*., The viscosity of atmospherically relevant organic particles. *Nat. Commun.* **9**, 956 (2018).
26. Á. Tóth *et al*., Chemical characterization of laboratory-generated tar ball particles. *Atmos. Chem. Phys.* **18**, 10407–10418 (2018).
27. C. Li *et al*., Dynamic changes in optical and chemical properties of tar ball aerosols by atmospheric photochemical aging. *Atmos. Chem. Phys.* **19**, 139–163 (2019).
28. B. Schmid *et al*., The DOE ARM aerial facility. *Bull. Am. Meteorol. Soc.* **95**, 723–742 (2014).
29. L. I. Kleinman *et al*., The time evolution of aerosol composition over the Mexico City plateau. *Atmos. Chem. Phys.* **8**, 1559–1575 (2008).
30. P. R. Buseck, K. Adachi, A. Gelencsér, É. Tompa, M. Pósfai, Ns-soot: A material-based term for strongly light-absorbing carbonaceous particles. *Aerosol Sci. Technol.* **48**, 777–788 (2014).
31. K. Adachi, S. H. Chung, P. R. Buseck, Shapes of soot aerosol particles and implications for their effects on climate. *J. Geophys. Res. Atmos.* **115**, D15206 (2010).
32. A. V. Tivanski, R. J. Hopkins, T. Tyliszczak, M. K. Gilles, Oxygenated interface on biomass burn tar balls determined by single particle scanning transmission X-ray microscopy. *J. Phys. Chem. A* **111**, 5448–5458 (2007).
33. R. J. Hopkins, A. V. Tivanski, B. D. Marten, M. K. Gilles, Chemical bonding and structure of black carbon reference materials and individual carbonaceous atmospheric aerosols. *J. Aerosol Sci.* **38**, 573–591 (2007).
34. B. Wang *et al*., Airborne soil organic particles generated by precipitation. *Nat. Geosci.* **9**, 433–437 (2016).
35. R. E. O'Brien *et al*., Physical properties of ambient and laboratory-generated secondary organic aerosol. *Geophys. Res. Lett.* **41**, 4347–4353 (2014).
36. J. Li, M. Pósfai, P. V. Hobbs, P. R. Buseck, Individual aerosol particles from biomass burning in southern Africa: 2. Compositions and aging of inorganic particles. *J. Geophys. Res. Atmos.* **108**, 8484 (2003).
37. K. Adachi, N. Moteki, Y. Kondo, Y. Igarashi, Mixing states of light-absorbing particles measured using a transmission electron microscope and a single-particle soot photometer in Tokyo, Japan. *J. Geophys. Res. Atmos.* **121**, 9153–9164 (2016).
38. P. Lin *et al*., Molecular characterization of Brown carbon in biomass burning aerosol particles. *Environ. Sci. Technol.* **50**, 11815–11824 (2016).
39. C. J. Hennigan *et al*., Chemical and physical transformations of organic aerosol from the photo-oxidation of open biomass burning emissions in an environmental chamber. *Atmos. Chem. Phys.* **11**, 7669–7686 (2011).
40. S. Zhou *et al*., Regional influence of wildfires on aerosol chemistry in the western US and insights into atmospheric aging of biomass burning organic aerosol. *Atmos. Chem. Phys.* **17**, 2477–2493 (2017).
41. A. P. Grieshop, N. M. Donahue, A. L. Robinson, Laboratory investigation of photochemical oxidation of organic aerosol from wood fires 2: Analysis of aerosol mass spectrometer data. *Atmos. Chem. Phys.* **9**, 2227–2240 (2009).
42. N. M. Donahue, J. H. Kroll, S. N. Pandis, A. L. Robinson, A two-dimensional volatility basis set – Part 2: Diagnostics of organic-aerosol evolution. *Atmos. Chem. Phys.* **12**, 615–634 (2012).
43. A. Bertrand *et al*., Evolution of the chemical fingerprint of biomass burning organic aerosol during aging. *Atmos. Chem. Phys.* **18**, 7607–7624 (2018).
44. X. Chen *et al*., Characterization of organic nitrogen in aerosols at a forest site in the southern Appalachian Mountains. *Atmos. Chem. Phys.* **18**, 6829–6846 (2018).
45. J. L. Jimenez *et al*., Evolution of organic aerosols in the atmosphere. *Science* **326**, 1525–1529 (2009).
46. R. J. Yokelson *et al*., Emissions from biomass burning in the Yucatan. *Atmos. Chem. Phys.* **9**, 5785–5812 (2009).
47. M. Kuwata, S. T. Martin, Phase of atmospheric secondary organic material affects its reactivity. *Proc. Natl. Acad. Sci. U.S.A.* **109**, 17354–17359 (2012).
48. L. Renbaum-Wolff *et al*., Viscosity of α-pinene secondary organic material and implications for particle growth and reactivity. *Proc. Natl. Acad. Sci. U.S.A.* **110**, 8014–8019 (2013).
49. X. Liu *et al*., Airborne measurements of western U.S. wildfire emissions: Comparison with prescribed burning and air quality implications. *J. Geophys. Res. Atmos.* **122**, 6108–6129 (2017).
50. A. P. Bateman, H. Belassein, S. T. Martin, Impactor apparatus for the study of particle rebound: Relative humidity and capillary forces. *Aerosol Sci. Technol.* **48**, 42–52 (2013).
51. A. Pajunoja *et al*., Adsorptive uptake of water by semisolid secondary organic aerosols. *Geophys. Res. Lett.* **42**, 3063–3068 (2015).
52. T. A. Semeniuk *et al*., Hygroscopic behavior of aerosol particles from biomass fires using environmental transmission electron microscopy. *J. Atmos. Chem.* **56**, 259–273 (2007).
53. N. Bluvshtein *et al*., Broadband optical properties of biomass-burning aerosol and identification of brown carbon chromophores. *J. Geophys. Res. Atmos.* **122**, 5441–5456 (2017).
54. P. F. Liu *et al*., Ultraviolet and visible complex refractive indices of secondary organic material produced by photooxidation of the aromatic compounds toluene and m-xylene. *Atmos. Chem. Phys.* **15**, 1435–1446 (2015).
55. S. Collier *et al*., Regional influence of aerosol emissions from wildfires driven by combustion efficiency: Insights from the BBOP campaign. *Environ. Sci. Technol.* **50**, 8613–8622 (2016).
56. T. B. Onasch *et al*., Soot particle aerosol mass spectrometer: Development, validation, and initial application. *Aerosol Sci. Technol.* **46**, 804–817 (2012).
57. J. S. Olfert, J. Wang, Dynamic characteristics of a fast-response aerosol size spectrometer. *Aerosol Sci. Technol.* **43**, 97–111 (2009).
58. K. Adachi, Y. Zaizen, M. Kajino, Y. Igarashi, Mixing state of regionally transported soot particles and the coating effect on their size and shape at a mountain site in Japan. *J. Geophys. Res. Atmos.* **119**, 5386–5396 (2014).
59. C. D. Cappa, J. L. Jimenez, Quantitative estimates of the volatility of ambient organic aerosol. *Atmos. Chem. Phys.* **10**, 5409–5424 (2010).
60. K. Adachi, P. R. Buseck, Changes of ns-soot mixing states and shapes in an urban area during CalNex. *J. Geophys. Res. Atmos.* **118**, 3723–3730 (2013).
61. Y. Takahashi *et al*., Comparison of solid-water partitions of radiocesium in river waters in fukushima and chernobyl areas. *Sci. Rep.* **7**, 12407 (2017).